

Dynamic manifestation of exception points in a non-Hermitian continuous model with an imaginary periodic potential

Y. T. Wang, R. Wang,* and X. Z. Zhang†

College of Physics and Materials Science, Tianjin Normal University, Tianjin 300387, China

Exceptional points (EPs) are distinct characteristics of non-Hermitian Hamiltonians that have no counterparts in Hermitian systems. In this study, we focus on EPs in continuous systems rather than discrete non-Hermitian systems, which are commonly investigated in both the experimental and theoretical studies. The non-Hermiticity of the system stems from the local imaginary potential, which can be effectively achieved through particle loss in recent quantum simulation setups. Leveraging the discrete Fourier transform, the dynamics of EPs within the low-energy sector can be well modeled by a Stark ladder system under the influence of a non-Hermitian tilted potential. To illustrate this, we systematically investigate continuous systems with finite imaginary potential wells and demonstrate the distinctive EP dynamics across different orders. Our investigation sheds light on EP behaviors, potentially catalyzing further exploration of EP phenomena across a variety of quantum simulation setups.

I. INTRODUCTION

The establishment of quantum mechanics is based on the Hermiticity of the Hamiltonian operator, which ensures the reality of the eigenvalues and the orthogonality of the eigenvectors. However, this mathematical framework is typically used to analyze closed systems that conserve energy and probability. In 1998, the pioneering work [1] by Bender demonstrated that a class of non-Hermitian Hamiltonians with parity-time reversal symmetry can possess a fully real spectrum. Subsequently, Ali [2] illustrated that pseudo-Hermitian operators are crucial for realizing the reality of the spectrum. Recently, non-Hermitian systems have been simulated in various physical systems, spanning from atomic [3–6] to photonic [7–11] platforms. Despite their ability to exhibit real spectra, these systems are not closed, allowing for energy and particle exchange with the environment. Disruption of the balance between the system and its environment leads to the emergence of a complex spectrum. Within this process, a critical region must exist where typical dynamic behavior is altered, accompanied by the appearance of an EP [12, 13]. Furthermore, the development of non-Hermitian topological phases [14] has introduced a new dimension to traditional condensed matter physics and quantum optics, reshaping our understanding of matter [14–22].

Recent advancements in experimental dissipation manipulation have reignited interest in studying open quantum systems, where dissipative processes are fundamental for quantum state preparation [23–25]. Specifically, experimental employment of dissipative coupling can achieve Tonks-Girardeau gas of molecules [26] and topological states [27], probing peculiar dynamical behaviors tied to passive parity-time symmetry in dissipative quantum systems [28–31]. The ability to simulate non-

Hermitian systems in open quantum setups has led to a series of discoveries, including non-Hermitian skin effects [32–36] and topological classifications exceeding the standard ten classes [37–41]. Recent studies have unveiled distinct dynamic traits of non-Hermitian skin effects in dissipative systems [4, 5, 10, 42, 43], alongside the appearance of chiral damping [44], helical damping [45], and edge bursts [46]. The motion of electrons in a lattice under an electric field is often elucidated by the Stark ladder model, involving a linear potential. This model is feasible in a tilted optical lattices [47, 48], showcasing intriguing phenomena like Bloch oscillations [49, 50], Zener tunneling [51, 52], and many-body Stark localization [53, 54]. Recent research has explored the Stark ladder model influenced by dissipative imaginary linear potentials, broadening the horizons of conventional Stark ladder model investigations [55].

When addressing problems in continuous quantum systems, it is necessary to discretize the system to a moderate extent to facilitate computation by computers. The Fourier grid Hamiltonian (FGH) method maps the kinetic and potential energy components of the Hamiltonian onto grid points in coordinate space. Through Fourier transformations, it ultimately yields a sum of cosine functions for each matrix element of the Hamiltonian in coordinate space [56]. It has proved a remarkably easy and robust method for computing the vibrational motion of one-dimensional systems [57, 58]. Systems processed with the FGH method more closely approximate real physical systems and thus have significant reference value for experiments. However, the application of the FGH method to the treatment of non-Hermitian quantum systems remains unexplored.

In this study, we expand the FGH method to encompass non-Hermitian continuous systems influenced by tilted imaginary potentials. Within the low-energy sector, dynamics are effectively modulated by a non-Hermitian tight-binding system, enabling the identification of EPs. We observe distinct orders of EPs within continuous systems featuring various wells. Notably, a

* wangr@tjnu.deu.cn

† zhangxz@tjnu.edu.cn

two-order EP, termed a scale-free EP, remains unchanged with increasing system size. The different EP orders exhibit unique dynamic behaviors discernible through the growth of the total Dirac probability, following a power law linked to the EP order index. Our findings offer valuable insights into the EP dynamics of non-Hermitian continuous systems.

Our paper is organized as follows. In Sec. II, we expand the FGH method to non-Hermitian continuous systems. In Sec. III, we describe the coalescing states of effective tight-binding Hamiltonian by the discretization of continuous system. In Sec. IV, we demonstrate the existence of scale-free behavior of EPs in the effective Hamiltonian. In Sec. V, we discuss the different dynamical behaviors of EPs, including EP2 and EP3. A summary is given in Sec. VI.

II. DISCRETIZATION OF A NON-HERMITIAN CONTINUUM MODEL WITH COMPLEX POTENTIAL

First, we examine a single particle exposed to a complex potential, with the corresponding Hamiltonian expressed as

$$H = T + V(x), \quad (1)$$

where $T = p^2/2m$ denotes the kinetic energy, and $V(x) = V_0(x) - i\kappa x$ defines the complex potential. Here,

$$V_0(x) = \gamma \sin^2(\omega\pi x) + (bx)^a \quad (2)$$

where γ is the depth of the potential well, and $i\kappa x$ is a linear imaginary potential which can be realized through the lossy system. A higher value of γ results in a deeper potential well. The parameter ω controls the width of each potential well, determining both the width and the number of wells within a system of a specified length. The second term sets the boundaries for the potential, confining the well to the range of $x \in [-1, 1]$. This condition requires that $b \leq 1$, with the specific value dependent on the width and depth of each potential well. Notably, if the depth of each well increases and their width decreases, b tends towards 1 to ensure that the wells at the edge positions have the same width as those at other positions. For simplicity, a is chosen as a large, even number. Beyond the interval, i.e., $x \notin [-1, 1]$, this component tends to diverge, indicating an open boundary for the system. Further cases are illustrated in Fig. 1, which will be employed to show the subsequent interesting dynamics.

To discretize the system under consideration, we begin by expressing the Hamiltonian in coordinate representation, where the matrix element is defined as

$$\begin{aligned} \langle x|H|x' \rangle &= \frac{1}{2\pi} \int_{-\infty}^{+\infty} \exp[ik(x-x')] T_k dk \\ &+ V(x) \delta(x-x'), \end{aligned} \quad (3)$$

where $T_k = \hbar^2 k^2 / 2m$. Initially, we substitute the discretized value $x_n = n\Delta x$ for the continuous variable x , where $n = 0, 1, 2, \dots, N' - 1$, N' represents the number of discrete points. Here, $\Delta x = L / (N' - 1)$ denotes the spacing between adjacent points, with L being the length of the system. The total length L and the spacing Δx determine the size of the reciprocal lattice and also establish the maximum wavelength value. Consequently, the expression for the reciprocal lattice in momentum space is

$$\Delta k = 2\pi/L = 2\pi / (N' - 1) \Delta x. \quad (4)$$

For convenience, we designate the center coordinate of the momentum space grid as $k = 0$, ensuring a symmetric distribution of grid points around $k = 0$. To maintain this symmetry, we opt for an odd number of discrete grid points N' in the coordinate space. Correspondingly, the discretization in the momentum space can be given by $k_l = l\Delta k$, where $-\tau \leq l \leq \tau$, $\tau = (N' - 1)/2$. In the discretization process, the identity operator is rewritten as

$$\hat{I}_x = \sum_{n=1}^{N'} |x_n\rangle \Delta x \langle x_n|, \quad (5)$$

which satisfies $\Delta x \langle x_n | x_{n'} \rangle = \delta_{nn'}$. By converting the integral into a summation and substituting Δx and Δk into the Eq. (3), we can obtain

$$\begin{aligned} H_{nn'} &= \frac{2}{\Delta x} \left\{ \sum_{l=1}^{\tau} \cos[2\pi l(n-n') / (N'-1)] T_l / (N'-1) \right. \\ &\left. + V(x_n) \delta_{nn'} \right\}, \end{aligned} \quad (6)$$

where $T_l = (\hbar l \Delta k)^2 / (2m)$. It is assumed here that $H_{nn'}$ with respect to $l = 0$ point.

Next, we turn to investigate the discretized state of the system. In the continuous limit, the eigenstates of the Hamiltonian H and its adjoint H^\dagger in coordinate representation are denoted as $\langle x|\psi\rangle = \psi(x)$ and $\langle x|\bar{\psi}\rangle = \bar{\psi}(x)$, respectively. The biorthonormalization condition is expressed as

$$\int_{-\infty}^{\infty} \bar{\psi}^*(x) \psi(x) dx = 1. \quad (7)$$

During the discretization process, this expression transforms into

$$\sum_{n=1}^{N'} \bar{\psi}^*(x_n) \psi(x_n) \Delta x = 1. \quad (8)$$

Similarly, the wavefunction in coordinate space is given by $\langle x_n|\psi\rangle = \psi(x_n) = \psi_n$ ($\langle x_n|\bar{\psi}\rangle = \bar{\psi}(x_n) = \bar{\psi}_n$). Consequently, we have

$$|\psi\rangle = \hat{I}_x |\psi\rangle = \sum_{n=1}^{N'} |x_n\rangle \Delta x \psi_n \quad (9)$$

and

$$|\bar{\psi}\rangle = \hat{I}_x |\psi\rangle = \sum_{n=1}^{N'} |x_n\rangle \Delta x \bar{\psi}_n. \quad (10)$$

The corresponding eigenenergy can be given as

$$E = \frac{\langle \bar{\psi} | H | \psi \rangle}{\langle \bar{\psi} | \psi \rangle} = \frac{\sum_{nn'} \bar{\psi}_n^* \Delta x H_{nn'} \Delta x \psi_n}{\Delta x \sum_n |\bar{\psi}_n \psi_n|}. \quad (11)$$

In this regard, the Eq. (6) can be reformulated as

$$H_{nn'}^0 = 2 \sum_{l=1}^{\tau} \cos[2\pi l (n - n') / (N' - 1)] T_l / (N' - 1) + V(x_n) \delta_{nn'}, \quad (12)$$

where $T_l = 2\{\hbar\pi l / [(N' - 1) \Delta x]\}^2 / m$. Referring to Eq. (12), the expectation value of $H_{nn'}^0$ is rewritten as

$$E = \frac{\sum_{nn'} \bar{\psi}_n^* H_{nn'}^0 \psi_n}{\sum_n |\bar{\psi}_n \psi_n|}. \quad (13)$$

At this stage, the discretization of the continuous system is complete, and the matrix elements of the discretized Hamiltonian can be solved using Eq. (12). When discretizing a continuous system with N' grid points, we transform the Hamiltonian into an N' order matrix, yielding N' eigenvalues and N' eigenvectors. Typically, increasing the number of grid points N' leads to more precise results. The choice of N' is also influenced by the form of the potential energy $V_0(x)$. In cases where the discretization length contains multiple potential wells, a larger N' ensures that the grid is fine enough to capture the details of each well.

III. EFFECTIVE HAMILTONIAN AND COALESCING STATES

In the domain of periodic potentials, the band structure manifests when particles are exposed to such potentials. Within the single-band approximation, the system can exhibit N low-lying eigenenergies that are notably distinct from the remaining eigenenergies by a discernible gap. This distinguishing feature persists even in the presence of a complex potential. Our attention is directed towards this low-lying eigenspectrum. Particularly noteworthy is the potential for eigenenergies to merge as the strength of the imaginary potential κ is varied, leading to the emergence of the EP in the spectrum. This intriguing behavior is illustrated in Figs. 2(a1-c1). Fig. 2(a1) distinctly depicts that when $\kappa = 0$, the reality of the low-lying energy spectrum remains intact. As κ surpasses κ_{c1} , imaginary energies emerge from the two lowest energies. When κ exceeds κ_{c2} , the real component diminishes, causing these conjugate pairs to separate into four imaginary eigenenergies.

To ascertain whether the eigenstates coalesce, we define the discretized eigenstate as

$$|\psi_q\rangle = \sum_{n=1}^{N'} d_q(n) |x_n\rangle, \quad (14)$$

and the fidelity between these states is given by

$$f_{qq'} = \frac{1}{\Omega_q \Omega_{q'}} \sum_{n=1}^{N'} |d_q(n)| |d_{q'}(n)|, \quad (15)$$

where q and q' are indices that depict the ordering of the imaginary components in the low-lying spectrum of the continuous system post discretization. Here, q ($q' = 1, 2, \dots, 2\omega + 1$ and the normalization factor is denoted as $\Omega_{q(q')} = \sqrt{\sum_n |d_{q(q')}(n)|^2}$. In Fig. 3, we numerically examine the overlap of the eigenstates in the low-lying spectrum of the discretized Hamiltonian H . The system parameters are consistent with those shown in Fig. 2. The yellow shaded region indicates instances where $f_{qq'} = 1$. The self-overlap along the diagonal represents a trivial region, while the non-diagonal yellow region signifies a non-trivial region. Notably, an EP2 is observed in the case of $N = 5$. Additionally, an EP3 is observed in the cases of $N = 7$ and 15.

To streamline the ensuing discussion, let us first derive the effective Hamiltonian concerning the low-lying spectrum. In the spirit of the tight-binding approximation, the eigenstates within the low-lying spectrum of H and H^\dagger can be given as

$$|\psi_n\rangle = \sum_{n'=1}^{N'} a_{n,n'} |x_{n'}\rangle = \sum_{l=1}^N d_{n,l} |\chi_l\rangle, \quad (16)$$

and

$$|\bar{\psi}_n\rangle = \sum_{n'=1}^{N'} \bar{a}_{n,n'} |x_{n'}\rangle = \sum_{l=1}^N \bar{d}_{n,l} |\chi_l\rangle, \quad (17)$$

where $n = 1, 2, 3, \dots, N$ complying with the biorthonormal relation $\langle \bar{\psi}_m | \psi_n \rangle = \delta_{mn}$. The initial equality in the above expressions suggests that the low-lying eigenstate can be expanded using a set of discretized states $|x_{n'}\rangle$ in the coordinate space. The subsequent equality indicates that the low-lying eigenstate can be obtained by combining the normalized ground state $|\chi_l\rangle$ of l -th equivalent single-well systems, essentially through a linear combination of N Wannier functions. By introducing the projection operator

$$P = \sum_{l=1}^N |\chi_l\rangle \langle \chi_l|, \quad (18)$$

and subsequently applying it to the Eq. (12). The effective Hamiltonian in the $\{|\chi_l\rangle\}$ representation can be

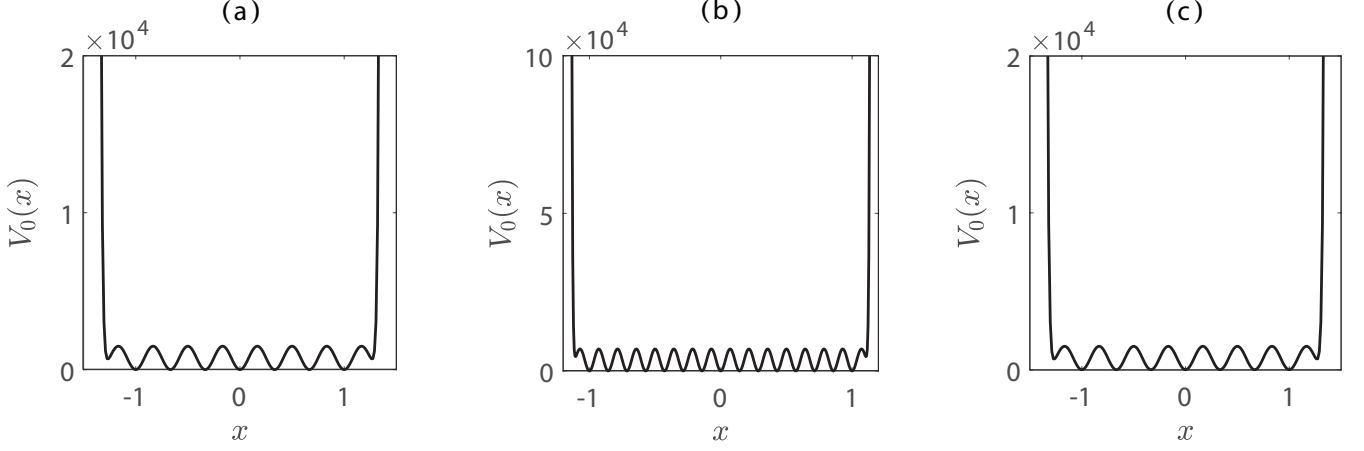


FIG. 1. (Color online) The continuum system comprises N potential wells created by $V_0(x)$ with the imaginary potential omitted from this representation. Figs. 1(a)-(c) correspond to the system with $N = 5, 7,$ and 15 potential wells, respectively. The specific parameter values for each system are as follows: (a) $N' = 201, L = 3, \omega = 2, \gamma = 800, b = 0.76, a = 80$; (b) $N' = 201, L = 3, \omega = 3, \gamma = 1500, b = 0.83, a = 100$; (c) $N' = 401, L = 2.3, \omega = 7, \gamma = 7000, b = 0.935, a = 200$.

given as

$$\begin{aligned} h_{\text{eff},ll'} &= \sum_{m',n'}^{N'} \langle \chi_l | P^{-1} | x_{m'} \rangle H_{m'n'}^0 \langle x_{n'} | P | \chi_{l'} \rangle \\ &= \sum_{n=1}^N E_n \langle \chi_l | \psi_n \rangle \langle \bar{\psi}_n | \chi_{l'} \rangle. \end{aligned} \quad (19)$$

After some straightforward algebras, the effective tight-binding Hamiltonian can be written as

$$H_{\text{eff}} = J_{\text{eff}} \sum_{j=1}^{N-1} (c_{j+1}^\dagger c_j + \text{h.c.}) + iF_{\text{eff}} \sum_{j=1}^N \left[\frac{-(N+1)}{2} + j \right] c_j^\dagger c_j, \quad (20)$$

where $c_j^\dagger (c_j)$ denotes the creation (annihilation) fermionic operator at the j -th site, and N denotes the length of the system. The effective hopping and tilted potential are given by

$$J_{\text{eff}} = \sum_{n=1}^N E_n \langle \chi_l | \psi_n \rangle \langle \bar{\psi}_n | \chi_{l+1} \rangle \quad (21)$$

and

$$F_{\text{eff}} = -i \sum_{n=1}^N \frac{E_n \langle \chi_l | \psi_n \rangle \langle \bar{\psi}_n | \chi_l \rangle}{-(N+1)/2 + l} \quad (22)$$

holds for any index value of $l = 1, 2, \dots, N$.

To simplify, we will omit the subscript of J_{eff} and F_{eff} in the following expressions. The Nambu expression of H_{eff} can be represented as

$$H_{\text{eff}} = \varphi^T h_{\text{eff}} \varphi, \quad (23)$$

where

$$h_{\text{eff}} = \begin{pmatrix} -2iF & J & 0 & 0 & 0 \\ J & -iF & J & 0 & 0 \\ 0 & J & 0 & J & 0 \\ 0 & 0 & J & iF & J \\ 0 & 0 & 0 & J & 2iF \end{pmatrix}, \quad (24)$$

and the base is represented as $\varphi = (c_1^\dagger, c_2^\dagger, \dots, c_5^\dagger)^T$. Considering the secular equation

$$h_{\text{eff}} \Psi_{\rho\sigma} = e_{\rho\sigma} \Psi_{\rho\sigma}, \quad (25)$$

one can determine the eigenenergies of the system as

$$e_{\rho\sigma} = \rho [(-5F^2 + 4J^2 + \sigma\Delta)/2]^{1/2}, \quad (26)$$

where $\Delta = [(2J^2 - 3F^2)^2 - 12J^2F^2]^{1/2}$. Here $\Xi_{\rho\sigma} = e_{\rho\sigma} + 2iF$, with $\rho(\sigma) = \pm, 0$, and $e_{++}, e_{+-}, e_{00}, e_{-+}, e_{--}$ are five eigenvalues of h_{eff} . The corresponding eigenstates are given by

$$\Psi_{\rho\sigma} = [1/(\Lambda_{\rho\sigma})^{1/2}] (\Theta_1, \Theta_2, \Theta_3, \Theta_4, \Theta_5)^T, \quad (27)$$

with the normalization coefficient being

$$\begin{aligned} \Lambda_{\rho\sigma} &= J^6 + |\Xi_{\rho\sigma}|^2 J^4 + |\Xi_{\rho\sigma} (\Xi_{\rho\sigma} - iF) J - J^3|^2 \\ &+ (|\Xi_{\rho\sigma}|^2 - 3F^2) (|\Xi_{\rho\sigma}|^2 - 2J^2)^2 [1 + J^2 (|\Xi_{\rho\sigma}|^{-2})], \end{aligned} \quad (28)$$

The other coefficients are listed as follow

$$\begin{aligned} \Theta_1 &= J^3, \\ \Theta_2 &= \Xi_{\rho\sigma} J^2, \\ \Theta_3 &= \Xi_{\rho\sigma} (\Xi_{\rho\sigma} - iF) J - J^3, \\ \Theta_4 &= (\Xi_{\rho\sigma} - iF) (e_{\rho\sigma} \Xi_{\rho\sigma} - 2J^2), \\ \Theta_5 &= J (\Xi_{\rho\sigma} - iF) [e_{\rho\sigma} \Xi_{\rho\sigma} - 2J^2] (\Xi_{\rho\sigma} - 4iF)^{-1} \end{aligned} \quad (29)$$

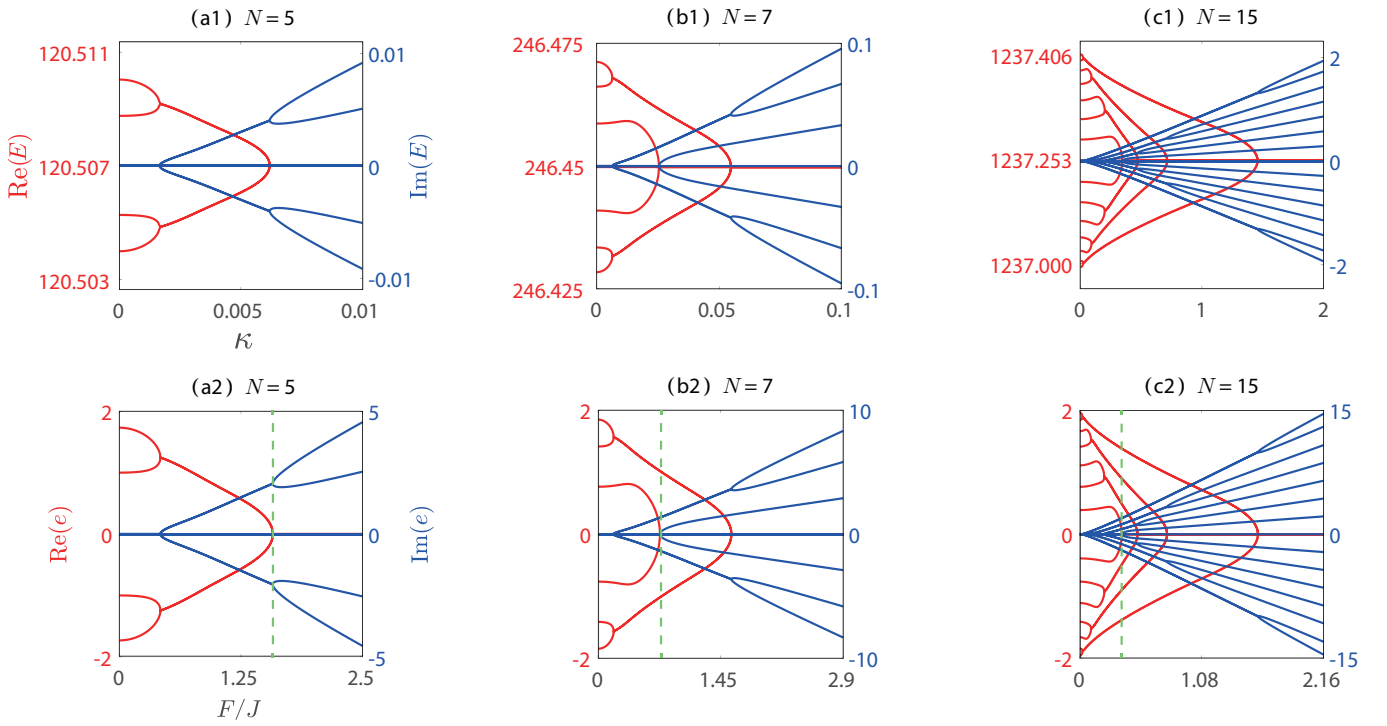


FIG. 2. (Color online) The low-lying spectrum of the discretized Hamiltonian H with the potential wells is depicted for $N = 5$ in (a1), $N = 7$ in (b1), and $N = 15$ in (c1), respectively. The red (blue) solid line represents the real (imaginary) part of the eigenenergy. Figs. 2(a2)-(c2) display the eigenspectrum of the effective tight-binding Hamiltonian H_{eff} . Clearly, the two spectra exhibit the same structure, demonstrating the accurate depiction of the low-lying structure of H by the tight-binding Hamiltonian H_{eff} . Notably, two eigenstates coalesce in (a1), while three eigenstates coalesce in both Figs. 2(b1)-(c1), corresponding to EP2 and EP3, respectively. This low-lying behavior is also evident in Figs. 2(a2)-(c2). Here, $J = 1$ is assumed for simplicity.

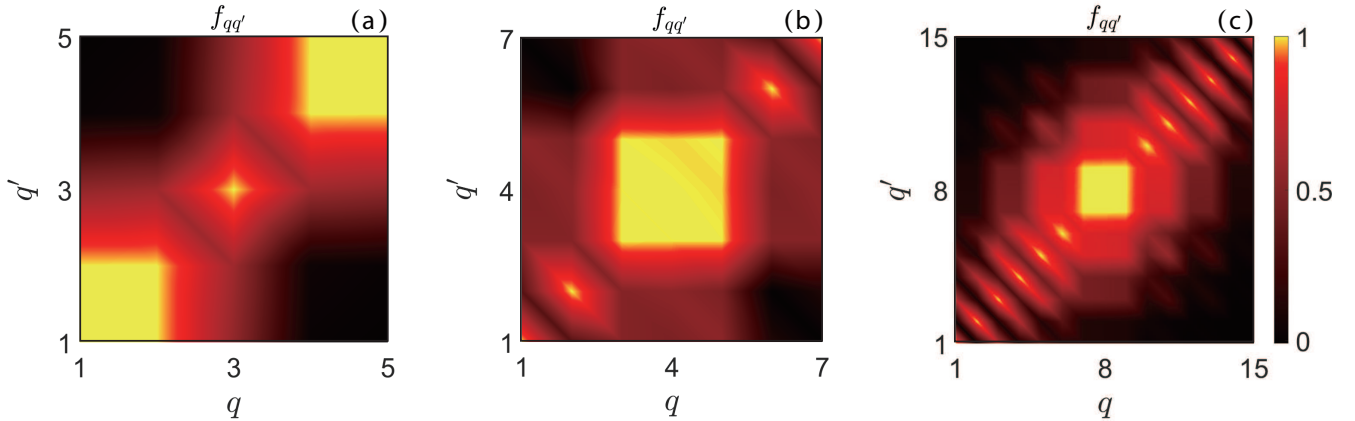


FIG. 3. (Color online) The overlap $f_{qq'}$ of the eigenstates within the low-lying spectrum of the discretized Hamiltonian H . The strengths of the loss are (a) $\kappa = 0.0062$, (b) $\kappa = 0.0252$, and (c) $\kappa = 0.3440$, respectively. The other system parameters within each panel are the same as those in the systems labeled by the green dashed lines in Figs. 2(a2)-(c2), respectively.

Notice that when the system parameters satisfy $\Delta = 0$, and we can obtain the following relation

$$(F/J)_{c_1} = \pm[(6 + 3\sqrt{3})/2]^{-1/2} \approx \pm 0.423 \quad (30)$$

$$(F/J)_{c_2} = \pm[(6 - 3\sqrt{3})/2]^{-1/2} \approx \pm 1.577. \quad (31)$$

Evidently, two types of EP emerge in h_{eff} when $(F/J)_{c_1} \approx \pm 0.423$ and $(F/J)_{c_2} \approx \pm 1.577$. These are

illustrated in Fig. 2(a2) and are consistent with those in the low-lying spectrum of the discretized Hamiltonian H , and are further verified by the coalescence of the eigenstates. We also present numerical results for the cases of $N = 7$ and 15 in Figs. 2 (b2)-(c2). Additionally, three key features should be emphasized: (i) When $|F/J| \leq (F/J)_{c1}$, all the eigenvalues are real. (ii) When $(F/J)_{c1} < |F/J| \leq (F/J)_{c2}$, the eigenvalues become complex; (iii) When $|F/J| > (F/J)_{c2}$, the eigenvalues become imaginary, losing their real parts. The above three regions correspond to the dynamics discussed in the subsequent section.

So far, we determine the properties of EPs numerically and theoretically through the $N = 5$ non-Hermitian tight-binding model. Comparing Figs. 2(a1)-(c1) to Figs. 2(a2)-(c2), the low-lying spectrum of discretized Hamiltonian H shares the same structure with that of the non-Hermitian effective Hamiltonian H_{eff} . The other parameters are the same in Fig. 2.

IV. SCALE-FREE EP

In the previous section, it was demonstrated that the H_{eff} effectively describes the low-energy behavior of non-Hermitian continuous systems, particularly the EPs in the spectrum. In this section, it will be shown that the system can host an EP independent of the number of potential wells. We begin with the secular equation of the effective Hamiltonian

$$h_{\text{eff}}|\Phi\rangle = e|\Phi\rangle, \quad (32)$$

where the eigenstate $|\Phi\rangle$ can be expressed as

$$|\Phi_n\rangle = \sum_{j=1}^N \beta_j |j\rangle, \quad (33)$$

with $|j\rangle = c_j^\dagger |\text{Vac}\rangle$. Substituting the above equation into Eq. (32), the following recurrence relation can be derived

$$\beta_{j+1} + \beta_{j-1} = \frac{j-\xi}{\alpha} \beta_j, \quad (34)$$

where $\alpha = iJ/F$, and $\xi = \varepsilon/F + (N+1)/2$ with $\varepsilon = -ie$. Typically, the Bessel function satisfies the above recurrence relation

$$Z_{n+1}(x) + Z_{n-1}(x) = \frac{2n}{x} Z_n(x), \quad (35)$$

where $Z = \mathcal{J}$ (Y) represents the first (or second) Bessel function. It is important to note that the above equation remains valid for purely imaginary quantities (the proof is provided in Appendix A). The expansion coefficients β_j will be expressed in terms of a combination of Bessel functions as

$$\beta_j = A\mathcal{J}_{j-\xi}(2\alpha) + B\mathcal{Y}_{j-\xi}(2\alpha), \quad (36)$$

where the variables are transformed, i.e., $n \rightarrow j - \xi$, and $x \rightarrow 2\alpha$. The boundary condition of $\beta_0 = \beta_{N+1} = 0$ lead to the following equations

$$A\mathcal{J}_{-\xi}(2\alpha) + B\mathcal{Y}_{-\xi}(2\alpha) = 0, \quad (37)$$

and

$$A\mathcal{J}_{N+1-\xi}(2\alpha) + B\mathcal{Y}_{N+1-\xi}(2\alpha) = 0. \quad (38)$$

By combining the above two equations, we obtain

$$\mathcal{J}_{-\xi}(2\alpha)Y_{N+1-\xi}(2\alpha) - \mathcal{J}_{N+1-\xi}(2\alpha)Y_{-\xi}(2\alpha) = 0. \quad (39)$$

The order of the Bessel function ξ must be real such that the eigenvalues are imaginary numbers, which are determined by the zero points of the above function. As $\alpha \rightarrow 0$, and $j - \xi \rightarrow \infty$, we can obtain

$$\mathcal{J}_{j-\xi}(-i\alpha) = \frac{1}{\sqrt{2\pi}} (-ie\alpha/2)^{j-\xi} (j-\xi)^{-(j-\xi+\frac{1}{2})} \quad (40)$$

and

$$\mathcal{J}_{j-\xi}(\alpha) = i^{(j-\xi)} \mathcal{J}_{j-\xi}(-i\alpha). \quad (41)$$

By utilizing the asymptotic behavior of the Bessel function, which is detailed in Appendix B, we obtain

$$\mathcal{J}_{j-\xi}(2\alpha) = \frac{1}{\sqrt{2\pi}} (e\alpha)^{j-\xi} (j-\xi)^{-(j-\xi+\frac{1}{2})}, \quad (42)$$

and

$$\mathcal{Y}_{j-\xi}(2\alpha) = \sqrt{\frac{2}{\pi}} (e\alpha)^{-(j-\xi)} (j-\xi)^{j-\xi-\frac{1}{2}}. \quad (43)$$

This results in $|\mathcal{J}_{N+1-\xi}(2\alpha)| = 0$ and $|\mathcal{Y}_{N+1-\xi}(2\alpha)| \gg 1$. Therefore, the Eq. (39) is simplified to

$$\mathcal{J}_{-\xi}(2\alpha) = 0. \quad (44)$$

By differentiating Eq. (39) with respect to ξ , we have

$$\partial[\mathcal{J}_{-\xi}(2\alpha)Y_{N+1-\xi}(2\alpha) - \mathcal{J}_{N+1-\xi}(2\alpha)Y_{-\xi}(2\alpha)]/\partial\xi = 0, \quad (45)$$

and combining the asymptotic behavior, we immediately obtain the additional condition to determine the EP of the system

$$\partial\mathcal{J}_{-\xi}(2\alpha)/\partial\xi = 0. \quad (46)$$

Straightforward algebra shows that

$$\begin{aligned} \partial\mathcal{J}_{-\xi}(2\alpha)/\partial\xi &= -\frac{\pi\alpha^{-2\xi}}{2\Gamma^2(-\xi+1)} [Y_{-\xi}(2\alpha) - \cot(-\xi\pi) \times \\ &\mathcal{J}_{-\xi}(2\alpha)] {}_2F_3(-\xi, -\xi + \frac{1}{2}; -\xi + 1, -\xi + \\ &1, -2\xi + 1; -4\alpha^2) - \mathcal{J}_{-\xi}(2\alpha) \times [-\frac{1}{2\xi} - \\ &\psi(-\xi + 1) + \ln \alpha + \alpha^2/(\xi^2 - 1)] {}_3F_4(1, 1, \\ &\frac{3}{2}; 2, 2, 2 + \xi, -\xi + 2; -4\alpha^2), \end{aligned} \quad (47)$$

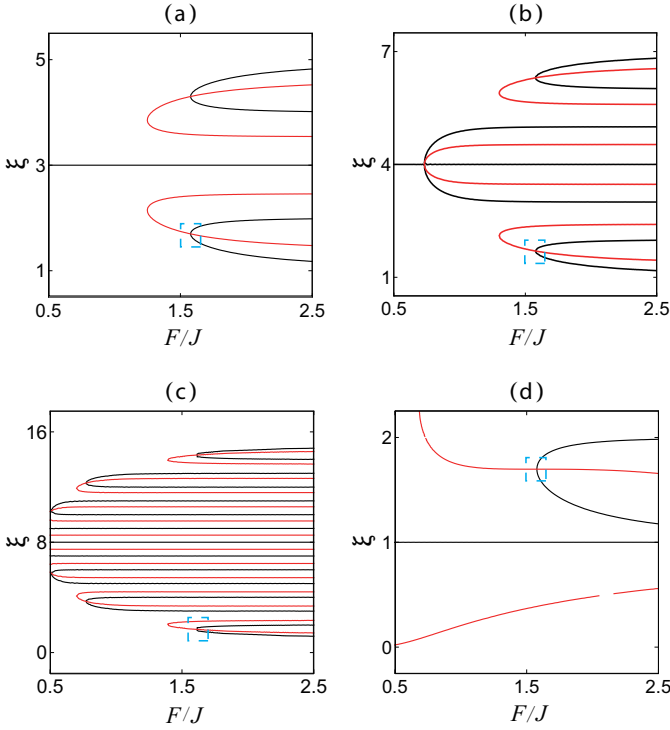


FIG. 4. (Color online) Plot of the solutions of ξ in Eqs. (39) and (45) as a function of F/J based on the analytical solution. Figs. 4(a)-(c) depict the cases of $N = 5, 7,$ and $15,$ respectively. The black and red solid lines represent the solutions of Eqs. (39) and (45), respectively. The intersection points within each figure indicate the EP of the system. While F/J decreases from infinity to a finite value, the first EP, denoted by the blue dashed line, always emerges at $(F/J)_{c_2} = 1.577.$ Fig. 4(d) showcases the zero solution of Eqs. (44) and (48), confirming that the theoretical solution of Eq. (48) in the limit of $\alpha \rightarrow 0,$ and $j - \xi \rightarrow \infty$ is independent of the system size. This independence suggests a scale-free EP at $(F/J)_{c_2} = 1.577$ with J assumed to be 1 for simplicity.

where ${}_pF_q$ represents the generalized hypergeometric function. By neglecting the last three terms, we obtain

$${}_2F_3(-\xi, -\xi + \frac{1}{2}; -\xi + 1, -\xi + 1, -2\xi + 1; -4\alpha^2) = 0. \quad (48)$$

It is crucial to highlight that the determination of Eq. (44) and Eq. (48) is independent of the system size $N,$ indicating a scale-free EP (the observation is presented in Fig. 4(d)). More details of the observations are further illustrated in Figs. 4(a)-(c), where the black and red solid lines correspond to the solutions of Eqs. (39) and (45), respectively. The intersection of these lines give rise to the EP of the system. The intersection point, denoted by the blue dashed rectangle, consistently occurs at $(F/J)_{c_2} = 1.577$ for $N = 5, 7,$ and 15 respectively. This uniform behavior is in line with our theoretical forecasts, indicating a universal trait.

V. THE DYNAMICS AT EP

Now, we shift our focus to the dynamics of the system. In the large N limit, the system's dynamics remain unaffected by the boundary condition due to the absence of the non-Hermitian skin effect. This leads us to consider a system with periodic boundary conditions for simplicity.

Before delving into a detailed analysis of EP dynamics, we first explore the system's dynamics significantly distant from the EP. It is imperative to highlight that the derivation of the propagator relies on an equidistant and complete real energy spectrum. In Figs. 5(a)-(b), we examine the energy spacing Δe of the Hamiltonian H_{eff} by adjusting $F/J.$ Two distinct regimes merit attention: (i) For $F/J < (F/J)_{c_1},$ the system exhibits a complete real spectrum without the characteristic of equidistant energy spacing. (ii) Conversely, for $F/J > (F/J)_{c_1},$ the system may showcase equidistant energy spacing alongside a complete imaginary energy spectrum. Upon considering the time evolution of the Hamiltonian $-iH_{\text{eff}},$ the presence of equidistant energy spacing and a complete real spectrum is confined to a specific parameter range, which will be the focal point of our subsequent discussion. By performing the Fourier transformation

$$c_j = \frac{1}{\sqrt{N}} \sum_k e^{ikj} c_k, \quad (49)$$

we rewrite the Eq. (20) in the form of

$$H_\xi(k) = -iH_{\text{eff}}(k), \quad (50)$$

where

$$H_{\text{eff}}(k) = \sum_k [2J \cos(k) - iF \frac{(N+1)}{2} - F \frac{\partial}{\partial k}] c_k^\dagger c_k. \quad (51)$$

Correspondingly, the eigenstate of $H_\xi(k)$ can be expressed as

$$|\psi(k)\rangle = \sum_k \psi(k) |k\rangle, \quad (52)$$

with $|k\rangle = c_k^\dagger |\text{Vac}\rangle.$ It fulfills the following secular equation

$$-i2J \cos(k) \psi(k) + iF \frac{\partial}{\partial k} \psi(k) = \xi \psi(k), \quad (53)$$

where $\xi = -ie + F(N+1)/2,$ and it is equidistant number. By utilizing the periodic boundary condition of the wavefunction $\psi(k + 2\pi) = \psi(k),$ we have

$$|\psi(k)\rangle = \frac{1}{\sqrt{N}} \sum_k \exp\{-i[i\frac{2J}{F} \sin(k) + \frac{\xi}{F}k]\} |k\rangle. \quad (54)$$

In the coordinate representation, it can be rewritten as

$$|\psi(m)\rangle = \frac{1}{N} \sum_{j,k} \exp\{-i[(m-j)k + \frac{2iJ}{F} \sin(k)]\} |j\rangle. \quad (55)$$

In the large N limit, the summation in the above can be replaced with an integral, yielding

$$|\psi(m)\rangle = \sum_j \mathcal{J}_{(m-j)}\left(-\frac{2iJ}{F}\right) |j\rangle. \quad (56)$$

Here, the Bessel Function of order n is expressed as

$$\mathcal{J}_n(z) = \frac{1}{2\pi} \int_{-\pi}^{\pi} \exp\{-i[n\theta - z \sin \theta]\} d\theta. \quad (57)$$

The dynamics of the system is fully captured by the propagator. However, the existence of the imaginary potential generally gives rise to an imaginary spectrum, which brings an exponentially growing total probability. To omit such divergence, we define $U(t) = \exp(-iH_\xi t)$ with $H_\xi = -iH_{\text{eff}}$ to observe the relative amplitude in each lattice site. In the coordinate space, the matrix element can be given as

$$U_{n'n}(t) = \mathcal{J}_{n'-n}\left[-\frac{4iJ}{F} \sin\left(-\frac{Ft}{2}\right)\right] e^{i(n'-n)(\pi-Ft)/2 - in'Ft} \quad (58)$$

wherein the property of the Bessel function

$$\sum_{k=-\infty}^{\infty} J_k(z) J_{k+p}(z) e^{ika} = J_p\left[2z \sin\left(\frac{a}{2}\right)\right] e^{ip(\pi-a)/2}, \quad (59)$$

is utilized. Evidently, it characterizes the periodic oscillation with period $T = 2\pi/F$. Fig. 6(a) showcases the time evolution of the total Dirac probability $P(t)$ for the Hamiltonian H_ξ with the system parameter $F/J = 4.3$. When the system satisfies the condition of equidistant energy spacing and a complete real spectrum, $P(t)$ exhibits oscillations with an approximate period of $T = 1.46$. The red empty circle and black solid line denote the analytical formula Eq. (58) and numerical results, respectively. However, for the effective Hamiltonian H_{eff} , satisfying such conditions proves challenging, regardless of the variations in the parameter F/J . Consequently, the

corresponding propagator fails to capture the system dynamics. In the region of a complete real spectrum, Figs. 5(c)-(d) illustrate the system dynamics for the system parameters $F/J = 0.2$, and 0.05 , respectively. In such region, the finite size effect precludes the emergence of a spectrum with equidistant energy spacing, leading to the disappearance of periodic behavior.

Next, we shift our focus to the EP dynamics of H_{eff} . The discussion is separated into three parts for clarity.

(i) When the system parameter satisfies the critical condition of $(F/J)_{c1} = [(6 + 3\sqrt{3})/2]^{-1/2} \approx 0.423$, the first EP emerges where two eigenstates coalesce. To elucidate the EP dynamics, we introduce the generalized eigenspace based on the Eqs. (24) and (25). The matrix representation h_{eff} transforms to

$$h_{\text{eff}}^{(B)} = S^{-1} h_{\text{eff}} S = \begin{pmatrix} e_{++} & 1 & 0 & 0 & 0 \\ 0 & e_{+-} & 0 & 0 & 0 \\ 0 & 0 & e_{00} & 0 & 0 \\ 0 & 0 & 0 & e_{-+} & 1 \\ 0 & 0 & 0 & 0 & e_{--} \end{pmatrix}, \quad (60)$$

where $S = (\varphi_{++}, \Phi_{+-}, \varphi_{00}, \varphi_{-+}, \Phi_{--})$ and the corresponding diagonal elements are $e_{++} = e_{+-} = 1.246$, and $e_{-+} = e_{--} = -1.246$. Here $\varphi_{++}(\varphi_{-+})$ is the generalized eigenvector of the eigenvector $\Phi_{+-}(\Phi_{--})$ following the relations

$$(h_{\text{eff}} - e_{++}I)\Phi_{+-} = \varphi_{++} \quad (61)$$

and

$$(h_{\text{eff}} - e_{-+}I)\Phi_{--} = \varphi_{-+}. \quad (62)$$

It is crucial to transform a non-Hermitian matrix with EPs into its standard Jordan block form. This transformation is essential because it allows for the derivation of the time-dependent amplitude through the systematic solution of decoupled differential equations. Straightforward algebraic operations reveal that

$$S = \begin{pmatrix} 0.041 - 0.329i & 0.494 - 0.058i & -0.436 & 0.041 + 0.329i & -0.494 - 0.058i \\ 0.329 - 0.376i & 0.705 + 0.016i & -0.368i & -0.329 - 0.376i & 0.705 - 0.016i \\ 0.529 & 0.707 & 0.591 & 0.529 & -0.707 \\ 0.329 + 0.376i & 0.705 - 0.016i & 0.368i & -0.329 + 0.376i & 0.705 + 0.016i \\ 0.041 + 0.329i & 0.494 + 0.058i & -0.436 & 0.041 - 0.329i & -0.494 + 0.058i \end{pmatrix}. \quad (63)$$

Note that the transformation matrix S is not unique and depends on the choice of the generalized eigenvector. Considering the time evolution of the arbitrary initial state $\psi(0) = [c_1(0), c_2(0), c_3(0), c_4(0), c_5(0)]^T$, the evolved state is governed by $h_{\text{eff}}^{(B)}$, i.e., $i\partial_t \psi = h_{\text{eff}}^{(B)} \psi$. The amplitude of the evolved state satisfies the following

system of differential equations

$$\begin{cases} i\partial_t c_1(t) = e_{++}c_1(t) + c_2(t) \\ i\partial_t c_2(t) = e_{+-}c_2(t) \\ i\partial_t c_3(t) = 0 \\ i\partial_t c_4(t) = e_{--}c_4(t) + c_5(t) \\ i\partial_t c_5(t) = e_{-+}c_5(t) \end{cases}, \quad (64)$$

leading to the solution

$$\psi(t) = \begin{pmatrix} c_1(0)e^{-1.246it} - ic_2(0)te^{-1.246it} \\ c_2(0)e^{-1.246it} \\ c_3(0) \\ c_4(0)e^{1.246it} - ic_5(0)te^{1.246it} \\ c_5(0)e^{1.246it} \end{pmatrix}. \quad (65)$$

Taking $c_j(0) = \delta_{j,3}$, and transforming it to the coordinate space $S^{-1}|\psi(t)\rangle$ results in

$$\psi(t) = \begin{pmatrix} -0.606e^{-1.246it} + 0.620ite^{-1.246it} \\ 0.620e^{-1.246it} \\ 1.293 \\ -0.606e^{1.246it} + 0.620ite^{1.246it} \\ -0.620e^{1.246it} \end{pmatrix}. \quad (66)$$

Evidently, the Dirac probability $P(t) = 3.175 + 0.769t^2$ increases with time t according to a power law. It is the evidence of the EP2, which is also demonstrated in Fig. 6(b).

(ii) When the system stays at the second EP, i.e., $(F/J)_{c_2} = [(6 - 3\sqrt{3})/2]^{-1/2} \approx 1.577$. The matrix form h_{eff} is given by

$$h_{\text{eff}} = \begin{pmatrix} -3.155i & 1 & 0 & 0 & 0 \\ 1 & -1.577i & 1 & 0 & 0 \\ 0 & 1 & 0 & 1 & 0 \\ 0 & 0 & 1 & 1.577i & 1 \\ 0 & 0 & 0 & 1 & 3.155i \end{pmatrix}, \quad (67)$$

Following the same procedures, we have

$$h_{\text{eff}}^{(B)} = S^{-1}h_0S = \begin{pmatrix} -2.054i & 1 & 0 & 0 & 0 \\ 0 & -2.054i & 0 & 0 & 0 \\ 0 & 0 & 0 & 0 & 0 \\ 0 & 0 & 0 & 2.054i & 1 \\ 0 & 0 & 0 & 0 & 2.054i \end{pmatrix}, \quad (68)$$

where

$$S = \begin{pmatrix} -0.639i & -0.117 & -0.132 & 0.015i & -0.029 \\ 0.703 & -0.768i & -0.416i & -0.079 & -0.139i \\ 0.303i & 0.454 & 0.787 & -0.303i & 0.454 \\ -0.079 & 0.139i & 0.416i & 0.703 & 0.768i \\ -0.015i & -0.029 & -0.132 & 0.639i & -0.117 \end{pmatrix}. \quad (69)$$

For an arbitrary initial state, its evolved state can be given as

$$\psi(t) = \begin{pmatrix} c_1(0)e^{-2.0543t} - ic_2(0)te^{-2.0543t} \\ c_2(0)e^{-2.0543t} \\ c_3(0) \\ c_4(0)e^{2.0543t} - ic_5(0)te^{2.0543t} \\ c_5(0)e^{2.0543t} \end{pmatrix}. \quad (70)$$

Taking $c_j(0) = \delta_{j,3}$, and transforming it to the coordinate space $S^{-1}|\psi(t)\rangle$ results in the Dirac probability $P(t) = [1.612 \cosh(4.109t)]t^2 - [1.128 \sinh(4.109t)]t + 1.810 \cosh(4.109t) + 6.497$, increasing with time t following a power law. Moreover, the analysis indicates that $(F/J)_{c_2} \approx 1.577$ represents the EP2. This phenomenon is further illustrated in Fig. 5(c).

(iii) Now we consider a high-order EP in a larger system. When $N = 7$, the system parameter $F/J \approx 0.732$ corresponding to the green dashed line in Fig. 2(b2) admits the following core matrix

$$h_{\text{eff}} = \begin{pmatrix} -2.196i & 1 & 0 & 0 & 0 & 0 & 0 \\ 1 & -1.464i & 1 & 0 & 0 & 0 & 0 \\ 0 & 1 & -0.732i & 1 & 0 & 0 & 0 \\ 0 & 0 & 1 & 0 & 1 & 0 & 0 \\ 0 & 0 & 0 & 1 & 0.732i & 1 & 0 \\ 0 & 0 & 0 & 0 & 1 & 1.464i & 1 \\ 0 & 0 & 0 & 0 & 0 & 1 & 2.196i \end{pmatrix}. \quad (71)$$

The eigenvalues are $e_1 = -A - iB$, $e_2 = A - iB$, $e_3 = A + iB$, $e_4 = e_5 = e_6 = 0$, and $e_7 = -A + iB$ where $A = 1.019$, $B = 1.337$. Obviously, there are three coalescent eigenstates in the above equation. Similarly, the standard

Jordan Block form is written as

$$h_{\text{eff}}^{(B)} = S^{-1}h_{\text{eff}}S = \begin{pmatrix} e_1 & 0 & 0 & 0 & 0 & 0 & 0 \\ 0 & e_2 & 0 & 0 & 0 & 0 & 0 \\ 0 & 0 & e_3 & 0 & 0 & 0 & 0 \\ 0 & 0 & 0 & e_4 & 1 & 0 & 0 \\ 0 & 0 & 0 & 0 & e_5 & 1 & 0 \\ 0 & 0 & 0 & 0 & 0 & e_6 & 0 \\ 0 & 0 & 0 & 0 & 0 & 0 & e_7 \end{pmatrix}, \quad (72)$$

where

$$S = \begin{pmatrix} -0.377 - 0.318i & 0.377 - 0.318i & 0.008 + 0.004i & 0.116i & -0.173 & -0.128i & -0.008 + 0.004i \\ 0.657 & 0.657 & -0.007 + 0.031i & -0.254 & -0.264i & 0.109 & -0.007 - 0.031i \\ -0.293 + 0.401i & 0.293 + 0.401i & -0.102 + 0.009i & -0.487i & 0.305 & 0.024i & 0.102 + 0.009i \\ -0.116 - 0.232i & -0.116 + 0.232i & -0.116 - 0.232i & 0.610 & 0 & 0.178 & -0.116 + 0.232i \\ 0.102 - 0.009i & -0.102 - 0.009i & 0.293 - 0.401i & 0.487i & 0.305 & -0.024i & -0.293 - 0.401i \\ -0.007 + 0.031i & -0.007 - 0.031i & 0.657 & -0.254 & 0.264i & 0.109 & 0.657 \\ -0.008 - 0.004i & 0.008 - 0.004i & 0.377 + 0.318i & -0.116i & -0.173 & 0.128i & -0.377 + 0.318i \end{pmatrix}. \quad (73)$$

Thus the evolved state can be given as

$$\psi(t) = \begin{pmatrix} c_1(0)e^{-ie_1t} \\ c_2(0)e^{-ie_2t} \\ c_3(0)e^{-ie_3t} \\ -c_6(0)\frac{t^2}{2} - ic_5(0)t + c_4(0) \\ -ic_6(0)t + c_5(0) \\ c_6(0) \\ c_7(0)e^{-ie_7t} \end{pmatrix}. \quad (74)$$

Taking $c_j(0) = \delta_{j,4}$, and transforming it to the coordinate space $S^{-1}|\psi(t)\rangle$ results in the Dirac probability $P(t) = 8.162t^4 + 29.627t^2 + 1.940 \cosh(2.674t) + 32.916$, increasing with time t following a power law. However, it scales proportionally to t^4 indicating the emergence of EP3. The numerical simulation is performed in Fig. 6(d).

VI. SUMMARY

In summary, we have systematically investigated the non-Hermitian continuous model, wherein non-Hermiticity arises from an imaginary on-site potential achievable through artificial synthetic systems. Within the low-energy sector, the spectrum of the system can transition from real to complex values. At the transition point, we have observed the presence of EPs, and their characteristics can be effectively modeled using a tilted imaginary potential within an adapted tight-binding Hamiltonian framework. Furthermore, the effective Hamiltonian can exhibit a scale-free EP, characterized by typical dynamic behavior. The growth of the total Dirac probability over time conforms to a power law, with its exponent determined by the order of the EP. These findings provide valuable insights into the dynamics of EPs within practical experiments and pave the way for exploring novel critical dynamic phenomena.

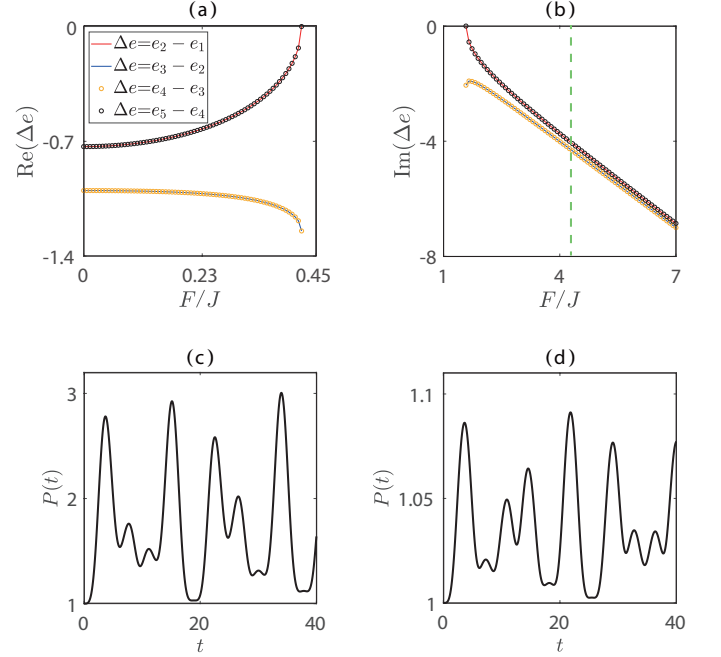


FIG. 5. (Color online) Energy spacing Δe and the total Dirac probability $P(t)$ of the effective Hamiltonian H_{eff} . Figs. 5(a)-(b) illustrate the full real and imaginary energy spectra as F/J varies. For $F/J > (F/J)_{c_2}$, the energy spectrum displays equidistant spacing, while this pattern is absent in other cases. The green dashed lines represent the situation when $F/J = 4.3$. Figs. 5(c)-(d) display the numerical variations of $P(t)$ with respect to t for the systems with $F/J = 0.2$, and 0.05 , respectively. The periodic behavior diminishes as the equidistant energy spacing is not present.

APPENDIX

A. Recurrence relation

Given the Bessel function defined by the differential equation

$$x^2 \frac{d^2 R}{dx^2} + x \frac{dR}{dx} + (x^2 - n^2)R = 0, \quad (75)$$

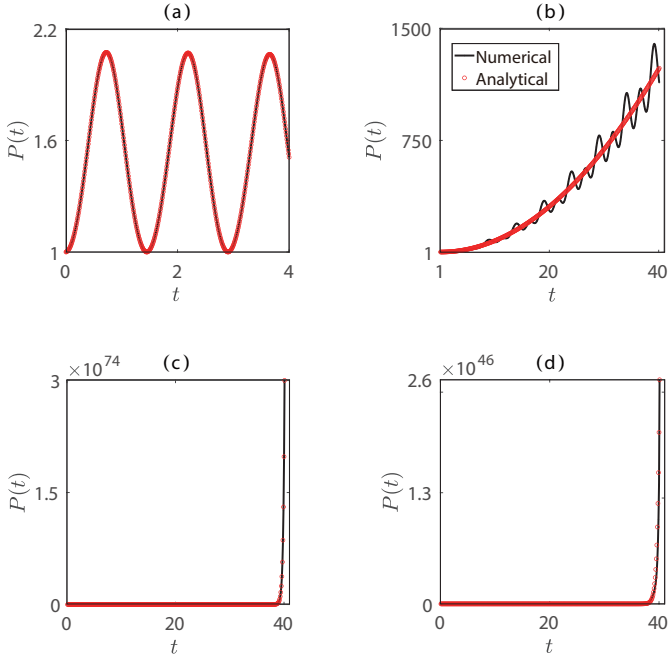


FIG. 6. (Color online) Plots illustrating of the Dirac probability $P(t)$ as a function of t . (a) For $F/J = 4.3$ ($N = 5$), representing the full real spectrum, $P(t)$ displays oscillations with a period $T \approx 1.46$. (b) At $(F/J)_{c_1} = 0.423$ ($N = 5$) and (c) $(F/J)_{c_2} = 1.577$ ($N = 5$), indicating the first and second EPs of the systems respectively, $P(t) \propto t^2$ exemplifies a power law behavior. (d) With $F/J = 0.732$ ($N = 7$). EP3 emerges as $P(t) \propto t^4$. The remaining system parameters align with those of the green dashed line in Fig. 2(b2). The red empty circle represents the analytical result, in good agreement with the numerical simulation depicted by the solid black line.

where n represents the order of the function. $\mathcal{J}_n(x)$ emerges as the solution to the n th-order Bessel function.

The series expression of the first kind Bessel function, denoted as $\mathcal{J}_n(x)$, is given by

$$\mathcal{J}_n(x) = \sum_{k=0}^{\infty} \frac{(-1)^k}{k!} \frac{1}{\Gamma(n+k+1)} \left(\frac{x}{2}\right)^{2k+n}, \quad (76)$$

Multiplying both sides of the above equation by x^n , and taking the first derivative with respect to x , we have

$$\frac{d}{dx} [x^n \mathcal{J}_n(x)] = nx^{n-1} \mathcal{J}_n(x) + x^n \mathcal{J}'_n(x) = x^n \mathcal{J}_{n-1}(x), \quad (77)$$

Similarly, we can obtain the relationship

$$\frac{d}{dx} [x^{-n} \mathcal{J}_n(x)] = -x^n \mathcal{J}_{n+1}(x). \quad (78)$$

By combining Eq. (77) and Eq. (78), and eliminating $\mathcal{J}'_n(x)$, we get

$$\mathcal{J}_{n+1}(x) + \mathcal{J}_{n-1}(x) = \frac{2n}{x} \mathcal{J}_n(x), \quad (79)$$

This recursive relation for $\mathcal{J}_n(x)$ holds true for any n .

Considering the second kind Bessel function,

$$Y_n(x) = \frac{\cos n\pi \mathcal{J}_n(x) - \mathcal{J}_{-n}(x)}{\sin n\pi}, \quad (80)$$

By substituting the series expression of $\mathcal{J}_n(x)$ into the above equation, we can show that $Y_n(x)$ also satisfies a recursive relation. Letting $\xi = ix$, we can rewrite the Bessel equation as

$$\xi^2 \frac{d^2 R}{dx^2} + \xi \frac{dR}{dx} - (\xi^2 + n^2) R = 0, \quad (81)$$

where $\mathcal{J}_n(\xi) = \mathcal{J}_n(ix)$, and its series expansion can be expressed as

$$\mathcal{J}_n(ix) = i^n \sum_{k=0}^{\infty} \frac{(-1)^k}{k!} \frac{1}{\Gamma(n+k+1)} \left(\frac{x}{2}\right)^{2k+n}. \quad (82)$$

The above expression indicates that the imaginary argument Bessel function

$$\mathcal{J}_n(ix) = i^n \mathcal{J}_n(x), \quad (83)$$

also satisfies the recursive relation of the real argument Bessel function.

B. Asymptotic behavior

Considering the series expression of the first kind Bessel function,

$$\mathcal{J}_n(x) = \sum_{k=0}^{\infty} \frac{(-1)^k}{k!} \frac{1}{\Gamma(n+k+1)} \left(\frac{x}{2}\right)^{2k+n}. \quad (84)$$

When $x \rightarrow 0$, the dominant term is given by

$$\mathcal{J}_n(x) = \frac{1}{\Gamma(n+1)} \left(\frac{x}{2}\right)^n, \quad (85)$$

where

$$\Gamma(n+1) = n^n e^{-n} (2\pi n)^{1/2} \left[1 + \frac{1}{12n} + o(n^{-2})\right]. \quad (86)$$

As $n \rightarrow \infty$, the expression simplifies to

$$\Gamma(n+1) = n^n e^{-n} (2\pi n)^{1/2}. \quad (87)$$

Therefore, the first kind Bessel function satisfies the relation

$$\mathcal{J}_n(x) = (2\pi n)^{-1/2} \left(\frac{ex}{2n}\right)^n, \quad (88)$$

where the parameters satisfy $x \rightarrow 0$, $n \rightarrow \infty$.

Similarly, the second kind Bessel function satisfies the relation

$$Y_n(x) = -\frac{\Gamma(n)}{\pi} \left(\frac{x}{2}\right)^{-n}, \quad (89)$$

Considering the recursive relation

$$n\Gamma(n) = \Gamma(n+1), \quad (90)$$

we can rewrite the second kind Bessel function as

$$Y_n(x) = \left(\frac{2}{\pi n}\right)^{1/2} \left(\frac{ex}{2n}\right)^{-n}. \quad (91)$$

ACKNOWLEDGMENTS

We acknowledge the support of the National Natural Science Foundation of China (Grants No. 12305026, No. 12275193).

-
- [1] C. M. Bender, and S. Boettcher, Real spectra in non-Hermitian Hamiltonians having \mathcal{PT} symmetry, *Phys. Rev. Lett.* **80**, 5243 (1998).
- [2] A. Mostafazadeh, Pseudo-Hermiticity versus \mathcal{PT} symmetry: the necessary condition for the reality of the spectrum of a non-Hermitian Hamiltonian, *J. Math. Phys.* **43**, 205 (2002).
- [3] I. Bloch, J. Dalibard, and W. Zwerger, Many-body physics with ultracold gases, *Rev. Mod. Phys.* **80**, 885 (2008).
- [4] Linhu Li, Ching Hua Lee, and Jiangbin Gong, Topological Switch for Non-Hermitian Skin Effect in Cold-Atom Systems with Loss, *Phys. Rev. Lett.* **124**, 250402 (2020).
- [5] Q. Liang, et al., Dynamic Signatures of Non-Hermitian Skin Effect and Topology in Ultracold Atoms, *Phys. Rev. Lett.* **129**, 070401 (2022).
- [6] Fang Qin, Ruizhe Shen, Linhu Li, and Ching Hua Lee, Kinked linear response from non-Hermitian cold-atom pumping, *Phys. Rev. A* **109**, 053311 (2024).
- [7] Liang Feng, Ramy El-Ganainy, and Li Ge, Non-Hermitian photonics based on parity-time symmetry, *Nat. Photonics* **11**, 752 (2017).
- [8] Mingsen Pan, Han Zhao, Pei Miao, Stefano Longhi, and Liang Feng, Photonic zero mode in a non-Hermitian photonic lattice, *Nat. Commun.* **9**, 1308 (2018).
- [9] S. K. Ödemir, S. Rotter, F. Nori, and L. Yang, Parity-time symmetry and exceptional points in photonics, *Nat. Mater.* **18**, 783 (2019).
- [10] Xueyi Zhu, et al., Photonic non-Hermitian skin effect and non-Bloch bulk-boundary correspondence, *Phys. Rev. Res.* **2**, 013280 (2020).
- [11] Aodong Li, et al., Exceptional points and non-Hermitian photonics at the nanoscale, *Nat. Nanotechnol.* **18**, 706 (2023).
- [12] T. Kato, *Perturbation Theory for Linear Operators*, Springer (1995).
- [13] W. D. Heiss, and A. L. Sannino, Avoided level crossing and exceptional points, *J. Phys. Math. Gen.* **23**, 1167 (1990).
- [14] E. J. Bergholtz, J. C. Budich, and F. K. Kunst, Exceptional topology of non-Hermitian systems, *Rev. Mod. Phys.* **93**, 015005 (2021).
- [15] S. Longhi, Parity-time symmetry meets photonics: A new twist in non-Hermitian optics, *Europhys. Lett.* **120**, 64001 (2017).
- [16] R. El-Ganainy, et al., Non-Hermitian physics and \mathcal{PT} symmetry, *Nat. Phys.* **14**, 11 (2018).
- [17] M.-A. Miri and A. Alu, Exceptional points in optics and photonics, *Science* **363**, eaar7709 (2019).
- [18] M. Parto, Y. G. N. Liu, B. Bahari, M. Khajavikhan, and D. N. Christodoulides, Non-Hermitian and topological photonics: optics at an exceptional point, *Nanophotonics* **10**, 403 (2020).
- [19] Y. Ashida, Z. Gong, and M. Ueda, Non-Hermitian physics, *Adv. Phys.* **69**, 249 (2020).
- [20] S. M. Zhang, X. Z. Zhang, L. Jin, and Z. Song, High order exceptional points in supersymmetric arrays, *Phys. Rev. A* **101**, 033820 (2020).
- [21] H. Wang, et al., Topological physics of non-Hermitian optics and photonics: a review, *J. Opt.* **23**, 123001 (2021).
- [22] K. Ding, C. Fang, and G. C. Ma, Non-Hermitian topology and exceptional-point geometries, *Nat. Rev. Phys.* **4**, 745 (2022).
- [23] F. Verstraete, M. M. Wolf, and J. Cirac, Quantum computation and quantum-state engineering driven by dissipation, *Nat. Phys.* **5**, 633 (2009).
- [24] M. Müller, S. Diehl, G. Pupillo, and P. Zoller, Engineered open systems and quantum simulations with atoms and ions, *Adv. At. Mol. Opt. Phys.* **61**, 1 (2012).
- [25] J. T. Barreiro, et al., An open-system quantum simulator with trapped ions, *Nature (London)* **470**, 486 (2011).
- [26] N. Syassen, et al., Strong dissipation inhibits losses and induces correlations in cold molecular gases, *Science* **320**, 1329 (2008).
- [27] S. Diehl, E. Rico, M. A. Baranov, and P. Zoller, Topology by dissipation in atomic quantum wires, *Nat. Phys.* **7**, 971 (2011).
- [28] J. Li, A. K. Harter, J. Liu, L. de Melo, Y. N. Joglekar, and L. Luo, Observation of parity-time symmetry breaking transitions in a dissipative Floquet system of ultracold atoms, *Nat. Commun.* **10**, 855 (2019).
- [29] M. Naghiloo, M. Abbasi, Y. N. Joglekar, and K. W. Murch, Quantum state tomography across the exceptional point in a single dissipative qubit, *Nat. Phys.* **15**, 1232 (2019).
- [30] L. Ding, K. Shi, Q. Zhang, D. Shen, X. Zhang, and W. Zhang, Experimental Determination of \mathcal{PT} -Symmetric Exceptional Points in a Single Trapped Ion, *Phys. Rev. Lett.* **126**, 083604 (2021).
- [31] L. Xiao, K. Wang, X. Zhan, Z. Bian, K. Kawabata, M. Ueda, W. Yi, and P. Xue, Observation of Critical Phenomena in Parity Time-Symmetric Quantum Dynamics, *Phys. Rev. Lett.* **123**, 230401 (2019).
- [32] T. E. Lee, Anomalous Edge State in a Non-Hermitian Lattice, *Phys. Rev. Lett.* **116**, 133903 (2016).
- [33] S. Yao and Z. Wang, Edge States and Topological Invariants of Non-Hermitian Systems, *Phys. Rev. Lett.* **121**, 086803 (2018).
- [34] F. K. Kunst, E. Edvardsson, J. C. Budich, and E. J. Bergholtz, Biorthogonal Bulk-Boundary Correspondence in Non-Hermitian Systems, *Phys. Rev. Lett.* **121**, 026808 (2018).
- [35] V. M. Martinez Alvarez, J. E. Barrios Vargas, and L. E. F. Foa Torres, Non-hermitian robust edge states in one dimension: Anomalous localization and eigenspace condensation at exceptional points, *Phys. Rev. B* **97**, 121401(R) (2018).

- [36] C. H. Lee and R. Thomale, Anatomy of skin modes and topology in non-hermitian systems, *Phys. Rev. B* **99**, 201103(R) (2019).
- [37] Z. Gong, Y. Ashida, K. Kawabata, K. Takasan, S. Higashikawa, and M. Ueda, Topological Phases of Non-Hermitian Systems, *Phys. Rev. X* **8**, 031079 (2018).
- [38] K. Kawabata, K. Shiozaki, M. Ueda, and M. Sato, Symmetry and Topology in Non-Hermitian Physics, *Phys. Rev. X* **9**, 041015 (2019).
- [39] H. Zhou and J. Y. Lee, Periodic table for topological bands with non-Hermitian symmetries, *Phys. Rev. B* **99**, 235112 (2019).
- [40] C.-H. Liu and S. Chen, Topological classification of defects in non-Hermitian systems, *Phys. Rev. B* **100**, 144106 (2019).
- [41] C.-H. Liu, H. Hu, and S. Chen, Symmetry and topological classification of Floquet non-Hermitian systems, *Phys. Rev. B* **105**, 214305 (2022).
- [42] S. Longhi, Unraveling the non-hermitian skin effect in dissipative systems, *Phys. Rev. B* **102**, 201103(R) (2020).
- [43] C.-H. Liu and S. Chen, Information constraint in open quantum systems, *Phys. Rev. B* **104**, 174305 (2021).
- [44] F. Song, S. Yao, and Z. Wang, Non-Hermitian Skin Effect and Chiral Damping in Open Quantum Systems, *Phys. Rev. Lett.* **123**, 170401 (2019).
- [45] C.-H. Liu, K. Zhang, Z. Yang, and S. Chen, Helical damping and dynamical critical skin effect in open quantum systems, *Phys. Rev. Res.* **2**, 043167 (2020).
- [46] W.-T. Xue, Y.-M. Hu, F. Song, and Z. Wang, Non-Hermitian Edge Burst, *Phys. Rev. Lett.* **128**, 120401 (2022).
- [47] M. B. Dahan, E. Peik, J. Reichel, Y. Castin, and C. Salomon, Bloch Oscillations of Atoms in an Optical Potential, *Phys. Rev. Lett.* **76**, 4508 (1996).
- [48] S. R. Wilkinson, C. F. Bharucha, K. W. Madison, Q. Niu, and M. G. Raizen, Observation of Atomic Wannier-Stark Ladders in an Accelerating Optical Potential, *Phys. Rev. Lett.* **76**, 4512 (1996).
- [49] F. Bloch, Über die Quantenmechanik der Electronen in Kristall gittern, *Z. Phys.* **52**, 555 (1929).
- [50] S. Longhi, Bloch Oscillations in Complex Crystals with \mathcal{PT} Symmetry, *Phys. Rev. Lett.* **103**, 123601 (2009).
- [51] C. Zener, A theory of electrical breakdown of solid dielectrics, *Proc. R. Soc. London A* **145**, 523 (1934).
- [52] S. Longhi, Non-Bloch-Band Collapse and Chiral Zener Tunneling, *Phys. Rev. Lett.* **124**, 066602 (2020).
- [53] M. Schulz, C. A. Hooley, R. Moessner, and F. Pollmann, Stark Many-Body Localization, *Phys. Rev. Lett.* **122**, 040606 (2019).
- [54] W. Morong, et al., Observation of stark many-body localization without disorder, *Nature (London)* **599**, 393 (2021).
- [55] Y. Zhang and S. Chen, Engineering an imaginary Stark ladder in a dissipative lattice: Passive \mathcal{PT} symmetry, K symmetry, and localized damping, *Phys. Rev. B* **107**, 224306 (2023).
- [56] C. Clay Marston and Gabriel G. Balint-Kurti, The Fourier grid Hamiltonian method for bound state eigenvalues and eigenfunctions, *J. Chem. Phys.* **91**, 3571 (1989).
- [57] Gabriel G. Balint-Kurti, et al., Grid methods for solving the Schrödinger equation and time dependent quantum dynamics of molecular photofragmentation and reactive scattering processes, *Int. Rev. Phys. Chem.* **11**, 317 (1992).
- [58] A. Macridin, P. Spentzouris, J. Amundson, and R. Harnik, Electron-Phonon Systems on a Universal Quantum Computer, *Phys. Rev. Lett.* **121**, 110504 (2018).